



Microstructure evolution of 316L stainless steel during solid-state additive friction stir deposition

Hossein Beladi, Ehsan Farabi, Peter D. Hodgson, Matthew R. Barnett, Gregory S. Rohrer & Daniel Fabijanic

To cite this article: Hossein Beladi, Ehsan Farabi, Peter D. Hodgson, Matthew R. Barnett, Gregory S. Rohrer & Daniel Fabijanic (2022) Microstructure evolution of 316L stainless steel during solid-state additive friction stir deposition, Philosophical Magazine, 102:7, 618-633, DOI: [10.1080/14786435.2021.2011980](https://doi.org/10.1080/14786435.2021.2011980)

To link to this article: <https://doi.org/10.1080/14786435.2021.2011980>



Published online: 12 Dec 2021.



Submit your article to this journal [↗](#)



Article views: 178



View related articles [↗](#)



View Crossmark data [↗](#)



Citing articles: 1 View citing articles [↗](#)



Microstructure evolution of 316L stainless steel during solid-state additive friction stir deposition

Hossein Beladi^a, Ehsan Farabi ^a, Peter D. Hodgson^a, Matthew R. Barnett^a, Gregory S. Rohrer^b and Daniel Fabijanic^a

^aInstitute for Frontier Materials, Deakin University, Geelong, Australia; ^bDepartment of Materials Science and Engineering, Carnegie Mellon University, Pittsburgh, PA, USA

ABSTRACT

Solid-state additive friction stir deposition was employed to three dimensionally print a 316L stainless steel. The microstructure, texture and grain boundary distribution were characterised using five-parameter boundary analysis. The bulk microstructure was exceptionally fine ($\sim 0.7 \mu\text{m}$) throughout the thickness of the deposited layers, consisting of equiaxed grains along with sub-grains delineated by high and low angle boundary segments. The misorientation angle distribution of the deposited layers was considerably different from the as-received microstructure, exhibiting a significant reduction in the relative areas of $\Sigma 3$ annealing twin boundaries due to their distortion by severe plastic deformation. The overall texture also exhibited strong shear components associated with FCC metals, suggesting that the microstructure refinement largely took place through progressive subgrain rotation, known as continuous dynamic recrystallisation. The grain boundary plane distribution revealed significantly lower anisotropy compared with the as-received material, showing two moderate peaks at the (111) and (110) orientations. The migration of high-angle mobile boundaries, which may have been induced by thermal cycle upon subsequent deposition along with the dislocation gradients between adjacent grains, slightly enhanced the intensity of low energy (111) orientations at the expense of (110) high-energy boundaries.

ARTICLE HISTORY



Received 28 July 2021
Accepted 23 November 2021

KEYWORDS

Additive stir friction deposition; continuous dynamic recrystallisation; grain boundary network; five-parameter analysis

Introduction

Additive manufacturing, commonly known as three-dimensional (3D) printing, has emerged as a step-change in metal manufacturing, where layer-by-layer metal deposition is employed to produce near net shape complex engineering components and minimise the use of machining. This emerging technology is revolutionising customisation and flexibility in metal processing,

CONTACT Hossein Beladi  hossein.beladi@deakin.edu.au  Institute for Frontier Materials, Deakin University, Geelong, Victoria 3216, Australia

providing an attractive pathway to manufacturing critical components. Fusion-based 3D printing technologies are currently the most common methods used in commercial applications. These technologies are, however, expensive to employ, requiring a close control over the feedstock, alloy design and processing parameters to achieve a uniform microstructure with acceptable properties [1, 2]. In addition, the grain sizes below 10 μm remain a challenge to achieve in these melt-based metal additive manufacturing processes.

Recently, several solid-state 3D printing technologies have been developed, analogous to forging in conventional metals processing, offering the potential to significantly refine the grain structure. The most mature technology is cold spray deposition, largely used as a repair process, since the bulk deposition through this technology suffers from porosity and high residual stress [3]. Therefore, a post heat treatment processing is needed to overcome these issues. This ultimately adds processing cost, complexity, and adversely coarsens the microstructure. Ultrasonic additive manufacturing is another emerging solid-state 3D printing technology, where stacks of very thin metal sheets ($\sim 100 \mu\text{m}$) are ultrasonically bonded to produce a bulk material with a limited size. However, this process requires a considerable post- or pre-machining of sheets to make complex shapes. In addition, there remains substantial issues with interlayer adhesion, again requiring high temperature treatment to rectify [4].

Additive friction stir deposition (AFSD) has emerged in recent years as a large-format additive manufacturing technology. In this process, a solid rod of input material contacts a plate/substrate and rotates under axial force to generate frictional heat. When sufficient heat is established, the input metal softens and shears at the tool shoulder. The metal softening, combined with a high frictional force between the rod and substrate (or previous layer), results in the deposition of a layer with a thickness of ~ 250 to $1000 \mu\text{m}$, depending on the metal and processing parameters [5]. This process was developed and commercialised by MELD Manufacturing in the USA, having a capability to print a volume of $0.3 \times 0.3 \times 1 \text{ m}^3$, and is readily scalable. High deposition rates and moderate print resolution ($\sim 10 \text{ mm}$) support the application to near net shape processing of large structural components [6].

The AFSD process has been successfully employed under different processing conditions for Al-Mg-Zn and Cu alloys, covering materials with low-to-high stacking fault energies. Although the mean grain size was reduced to $\sim 10 \mu\text{m}$ for both alloys, the SFE appeared to significantly influence the microstructure evolution mechanism through AFSD. The Al-Mg-Zn alloy with a high SFE displayed classical continuous dynamic recrystallisation, where the microstructure undergoes a progressive fragmentation through both geometric and local rotation of subgrain/s mechanisms. By contrast, the copper alloy with medium SFE exhibited conventional recrystallisation, through the nucleation and growth of new grains during/after deposition [7].

The work by Griffiths et al. [7] suggests that the mechanism of grain evolution in AFSD is largely governed by SFE over a wide processing window. However, Rivera et al. [8] demonstrated that the grain size can be further refined by about an order of magnitude ($\sim 1 \mu\text{m}$ on average) in an Inconel 625 alloy with a medium SFE through AFSD. The extreme grain refinement was ascribed to continuous dynamic recrystallisation, though no sufficient analysis was provided to support that. Therefore, this study aimed to replicate the AFSD process used in [8] to print 316L stainless steel, which is one of the most technologically important metals. Advanced electron microscopy techniques were extensively utilised in the current study to disclose the mechanism of grain refinement through a detailed examination of texture and grain boundary network characteristics throughout the thickness of a 3D print block of 316L stainless steel.

Experimental procedure

The material used in the current study was a commercial 316L stainless steel with a nominal composition of 13 Ni, 17 Cr, 1.5 Mn, 2 Mo, 0.05 C, 0.5 Si (in wt%). The as-received material was machined to obtain feedstock pins with a length of 300 mm having a cross-section of 10 mm \times 10 mm. The feedstock was then placed in the hollow rotating tungsten carbide tool as input material for the AFSD machine, known as MELD B8. The solid feedstock pin came in contact with the SS 316L as-received substrate, while rotating at a speed of 440 rpm under a normal force in a range of 9 kN to 18 kN, which varied with the feed rate. The feedstock pin moved horizontally forward and backward at an average rate of 25 mm per minute, while the material was deposited layer by layer on the substrate at an average rate of 2.5 mm per minute under an argon atmosphere. Each deposition layer had a dimension of ~ 100 mm length and ~ 20 mm width and thickness of ~ 0.5 mm. In total, 60 layers were deposited using two feedstock rods, obtaining a three-dimensional printed block with a height of 30 mm.

The microstructure characterisation was conducted using a scanning electron microscope equipped with an electron backscatter diffraction (EBSD) detector. The EBSD sample was prepared using a standard polishing routine followed by final polishing using a colloidal silica slurry solution. EBSD was conducted using a FEI Quanta 3D FEG FIB-SEM microscope, at 20 kV voltage and 4 nA current with a step size of 70 nm or 1 μm depending on the average grain size for the grain boundary characterisation.

EBSD maps for the grain boundary characterisation were acquired at two different cross-sections, namely parallel and perpendicular to the deposition direction, for a given layer to diminish the texture bias. The post-processing of data was performed by TSL-OIMTM software. The EBSD maps were subjected to a series of cleaning procedures for grain boundary characterisation;

namely grain dilation, a single average orientation per grain assignment and boundary reconstruction. The latter was used to extract the straight grain boundary line segments, which were interpreted stereologically to measure the grain boundary plane character distribution, an approach referred to as five-parameter analysis [9]. At least, 50,000 grain boundary line segments were required to reliably measure the grain boundary plane orientation.

EBSD maps for the texture measurement were acquired using a JEOL JSM 7800F FEG-SEM microscope at a step size of 0.5 μm on an area of 1500 $\mu\text{m} \times 1500 \mu\text{m}$ at different positions perpendicular to the deposited layers: (I) the edge, and (II) the middle. The post processing was conducted by means of the ATEX software [10] using monoclinic symmetry.

The fine microstructure of the deposited 316L was further analysed using the transmission Kikuchi diffraction (TKD) technique. The TKD samples were prepared by a similar preparation method used for transmission electron microscopy specimens. Thin foils with a thickness of 70 μm were prepared and twin-jet electropolished by A2 StruersTM electrolyte solution containing 6% perchloric acid at -20°C using a potential of 30 V. The FEG Quanta 3-D FEI SEM working under 30 kV and 8 nA using the Oxford Instruments TKD sample holder was employed for TKD measurements. An area of 15 $\mu\text{m} \times 15 \mu\text{m}$ with a step size of 20 nm was mapped using TSL software. The TKD post-processing was conducted using the TexSEM Laboratories Inc., software (TSL). The grain size was measured using the equivalent grain diameter approach. Statistical error was calculated using standard error = $\frac{S}{\sqrt{N}}$, where S and N are standard deviation and number of measurements, respectively.

Results and discussion

The as-received microstructure consisted of equiaxed grains with an average size of $32 \pm 0.9 \mu\text{m}$ (Figure 1(a)). The misorientation angle distribution revealed a prominent peak at the position of 60° for boundaries with their misorientation axes strongly clustered around the $\langle 111 \rangle$ direction in the standard stereographic triangle (Figure 1(b)). This suggests that first order annealing $\Sigma 3$ twin boundaries characterised by a $60^\circ/\langle 111 \rangle$ lattice misorientation represent a significant portion of the boundaries. The length fraction of $\Sigma 3$ boundaries was $46 \pm 0.5\%$ of the total length fraction considering 10° deviation angle from the ideal $60^\circ/\langle 111 \rangle$ lattice misorientation. Here, the $\Sigma 3$ boundaries having the grain boundary trace orientation within $\pm 10^\circ$ deviation from the trace expected for the ideal $\{111\}$ twin plane orientation were considered coherent $\Sigma 3$ boundaries. A 10° deviation angle ensures the presence of at least 2000 boundary segments for coherent/incoherent twin boundary types in the data set to reliably measure the grain boundary plane distribution [9]. For the as-

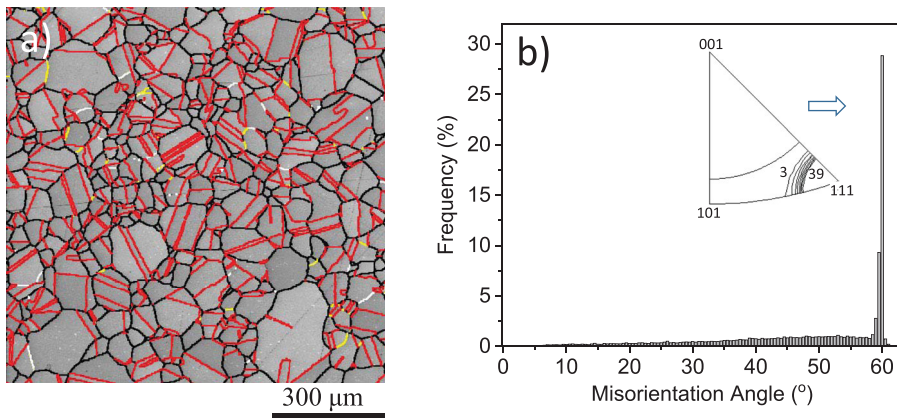


Figure 1. The band contrast EBSD image (a) and corresponding misorientation angle distribution along with the distribution of axes at a rotation angle of 60° in a standard stereographic triangle for the as-received (substrate) 316L stainless steel. The black, yellow, white, and red lines in (a) represent boundaries with misorientation angles $>15^\circ$, $>10^\circ$, $>5^\circ$ and twin boundaries (i.e. $60^\circ/\langle 111 \rangle$), respectively. To view this figure in colour, please visit the online version of the paper.

received microstructure, $40.9 \pm 0.5\%$ of all boundaries were coherent $\Sigma 3$ boundaries and $4.6 \pm 0.2\%$ were incoherent $\Sigma 3$ boundaries.

Feedstock pin. The overall microstructure of the feedstock pin after the deposition process significantly differed from the as-received condition, revealing two distinct microstructures. The region away from the feedstock tip (shown as region 'A' in Figure 2(a)) displayed coarse equiaxed grains, containing a significant fraction of fine/thin elongated bands whose misorientations were classified as $60^\circ/\langle 111 \rangle$ (i.e. red lines in Figure 2(b)). By contrast, the pre-existing annealing twins appeared to lose their lattice misorientation characteristics either fully or partially, representing distorted $\Sigma 3$ boundaries (shown by arrows in Figure 2(b)). The $\Sigma 3$ boundary distortion is known to occur through an interaction between extrinsic glide dislocations and the intrinsic

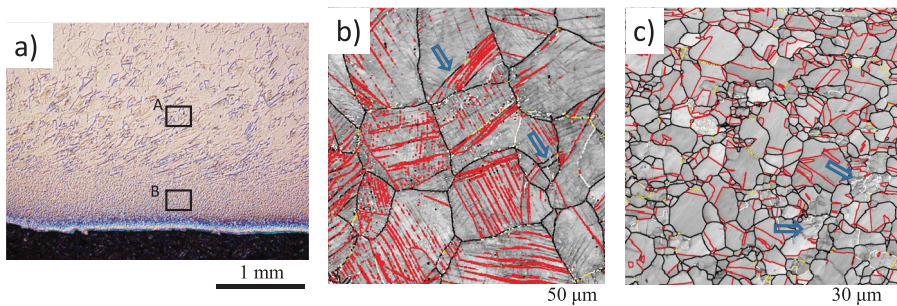


Figure 2. (a) The optical micrograph of feedstock pin cross section after deposition process. (b, c) band contrast EBSD images of region A in (a) and region B in (a), respectively. The black, yellow, white and red lines in (b, c) represent boundaries with misorientation angles $>15^\circ$, $>10^\circ$, $>5^\circ$ and twin boundaries with a lattice misorientation of $60^\circ/\langle 111 \rangle$, respectively. To view this figure in colour, please visit the online version of the paper.

dislocations within a twin boundary, which alters the dislocation network of the twin interface, changing the boundary misorientation angle and/or axis [11]. This suggests that the feedstock material was plastically deformed during the deposition process, which distorted the annealing twins and introduced intra-granular planar defects with the $60^\circ/\langle 111 \rangle$ misorientation, which are known as mechanical twins. The formation of mechanical twins is not surprising here, as the stacking fault energy of 316L is $\sim 60 \text{ mJ/m}^2$ [12], which hinders dislocation cross slip, leading to dislocation dissociation and promotion of mechanical twinning upon deformation [13]. Therefore, it appears that the normal force upon the feedstock during the deposition led to the formation of mechanical twins. However, the original grains appeared to maintain their equiaxed morphology despite the introduction of deformation. This is due to constraints imposed to the feedstock through the feedstock wall case and substrate. This introduces a condition in which the deformation/stress is uniformly distributed within the feedstock, similar to hydrostatic condition. As a result, the overall grain morphology is retained as equiaxed despite undergoing deformation. A similar result was reported for Hadfield steel subjected to explosion, where mechanical twins were introduced within grain interiors with no obvious change in the morphology of the initial equiaxed grains [14]. Despite the distortion of the annealing twin boundaries, the misorientation angle distribution exhibited a pronounced peak at 60° having $\langle 111 \rangle$ misorientation axis (Figure 3 (a)). In fact, the introduction of a large fraction of mechanical twins overshadowed the changes expected in the misorientation angle/axis distributions because of $\sum 3$ annealing twin boundary distortion.

The region within $\sim 1 \text{ mm}$ of the pin surface that was in contact with the deposited layer (i.e. 'B' in Figure 4(a)), revealed a distinct microstructure consisting of equiaxed grains with a much finer average grain size (i.e. $3.9 \pm 0.1 \mu\text{m}$, Figure 2(c)) compared with the overall pin microstructure/as-received condition (i.e. $32 \pm 0.9 \mu\text{m}$). The misorientation angle distribution was similar to

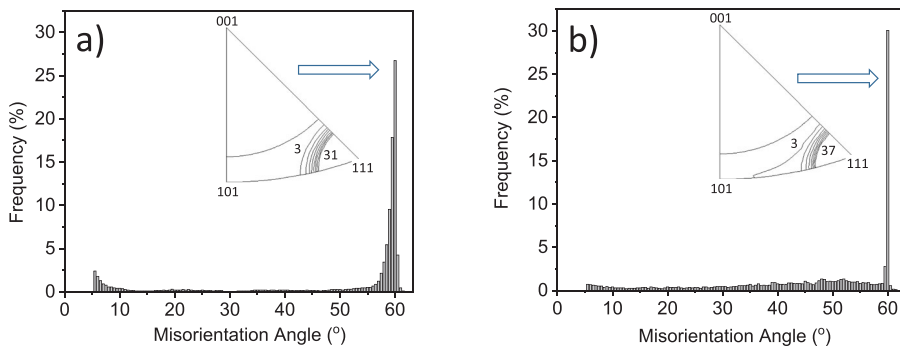


Figure 3. The misorientation angle distribution for feedstock pin at positions of (a) 'A' and (b) 'B' shown in Figure 2(a) and their corresponding distributions of misorientation axes at a rotation of 60° in a standard stereographic triangle.

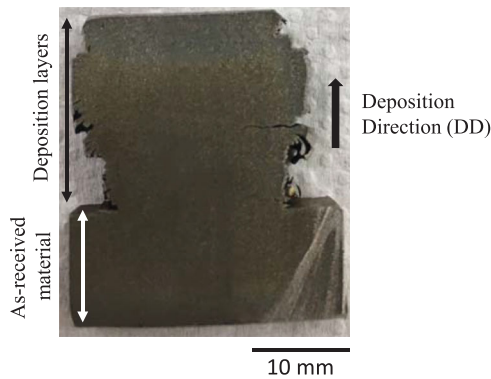


Figure 4. The cross section of multi-layer deposited 316L stainless steel using additive friction stir deposition.

the as-received condition, showing a distinct peak at 60° (Figure 3(b)). This is a classical recrystallised grain structure, suggesting that the temperature of pin was locally increased to such an extent that the deformed pin microstructure was recrystallised. This is not surprising, as there is extensive friction between the feedstock tip and substrate/deposited layer, which would lead to an increase in the feedstock temperature. It is expected that the temperature progressively increases at an early stage of processing and more or less becomes constant as the deposition continues. Interestingly, some of the grains had a relatively elongated morphology containing equiaxed substructure surrounded by low angle boundaries (shown by arrows in Figure 2(c)). This suggests that the fine equiaxed grains were continuously subjected to the straining during their evolution, as is also evident from the deviation in the misorientation axis distribution at 60° , where the maximum at $\langle 111 \rangle$ is broader than in the as-received microstructure and spreads towards $\langle 101 \rangle$ axis (Figure 3(b)). This is a typical characteristic of a microstructure undergoing discontinuous dynamic recrystallisation (DDRX, i.e. in which a nucleation and growth process is active), where the DDRX grains continuously undergo straining during their development, leading to substructure formation within the DRX grain interior and the distortion of the annealing twin boundaries (i.e. deviating from ideal misorientation angle/axis) [15]. The region of pin, which was in contact with substrate/deposited layer had a bright-blue contrast due to the oxidation, revealing a similar microstructure to region 'B' (Figure 2(a)).

Deposited layers. Multiple layers were successfully deposited through the additive friction stir deposition approach using the MELD apparatus. The cross-section of the deposited layers revealed some excess material laterally spreading after each layer deposition (Figure 4). In addition, a horizontal macro crack was apparent at the middle, where the deposition of the second feedstock was initiated. Figure 5(a) displays the ideal orientations in FCC metals subjected to shear deformation. The overall texture at the edge of

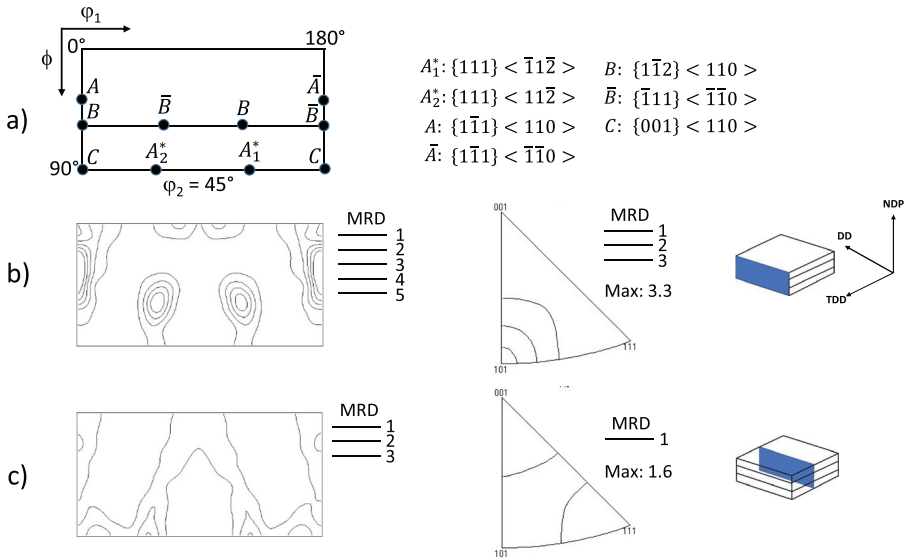


Figure 5. (a) Schematic representation of the main shear texture components for FCC materials in Euler space and their corresponding crystallographic orientations [16]. ODF section at $\varphi_2 = 45^\circ$ along with the inverse pole figures for the edge (b) and middle (c) of the deposited layers. MRD represent multiples of random distribution. NDP, DD and TDD are normal to print plane, print direction and transverse to print direction, respectively.

deposited layers revealed a moderate strength, having ~ 5 multiples of a random distribution (MRD). It largely composed of strong peaks at the positions of the B and \bar{B} orientations situated on the $\{hkl\}\langle 110 \rangle$ fibre and relatively weaker A and \bar{A} components located along the $\{111\}\langle uvw \rangle$. This is closely aligned with an ideal shear texture developed in FCC materials as a result of continuous lattice rotation where the $\langle 110 \rangle$ slip direction is along the shear direction (i.e. B fibre components) and/or the $\{111\}$ slip plane with the shear plane (i.e. A fibre components) [17]. The corresponding inverse pole figure is characterised by a moderate texture with a maximum of 3.3 MRD having the main peak at the $\langle 101 \rangle$ fibre position oriented along the shear direction (Figure 5(b)). Similar overall texture characteristics were reported for FCC materials subjected to high temperature torsion [18] and friction stir welding [19] and also ASFD of Al-Mg-Si alloy [7]. In other words, the dominant presence of A and B fibres suggests that the material experienced a large amount of shear deformation, as expected from the current deposition process.

The overall texture at the middle of the deposited layers differed significantly from the edge, having a weaker strength (≈ 3 MRD) and multiple peaks at the position of A^* and C . The C component emerges when the $\langle 110 \rangle$ slip direction is aligned with the shear direction and the $\{001\}$ plane with the shear plane [17]. As a result, the corresponding inverse pole figure displayed two peaks at $\langle 111 \rangle$ and $\langle 001 \rangle$ with a strength of ~ 1.6 MRD (Figure 5(c)). A similar observation was reported for austenitic stainless steel subjected to FSW, indicating that

the material experiences a distinct deformation path at different regions of deposition [20]. In other words, the edge of the deposited layers experiences pure shear and, as the distance from the edge towards the middle of the deposited layers increases, the deformation path becomes more complex.

To understand the homogeneity of the microstructure throughout the deposition, the microstructures of the first and last deposition layers were examined. The microstructure of the deposited layers consisted of very fine equiaxed grains, largely surrounded by high angle boundaries, along with subgrains delineated by low angle boundaries. The average grain sizes of the first and last layers were $0.76 \pm 0.06 \mu\text{m}$ and $0.66 \pm 0.05 \mu\text{m}$, respectively (Figure 6). The extent of grain refinement is similar to what was earlier reported for Inconel 625 alloy processed through AFSD [8]. Despite a small difference in the grain size between the first and last deposition layers, this process led to a significant grain refinement and somewhat homogenous distribution of grain size throughout the thickness of the build. This suggests that the thermal cycle generated through the subsequent deposition does not significantly alter the grain characteristics of previously deposited layers. In spite of these observations, the presence of dislocation recovery due to thermal cycling cannot be ruled out here, as it is expected to some extent to alter the dislocation arrangement within the microstructure, as discussed later.

Additive friction stir deposition is an extension of the friction stir welding process, where the material undergoes extensive plastic deformation (i.e. up to strains of 5) at an estimated strain rate of $2\text{--}12 \text{ s}^{-1}$ within a temperature range of warm-to-hot working condition (i.e. $0.5\text{--}0.9 T_m$, melting point in K), generated by friction heat [5]. The FSW process refines the grain size of the microstructure. It is believed that the grain refinement through FSW is a result of discontinuous dynamic recrystallisation (i.e. nucleation and growth) for medium-to-low SFE materials [21, 22]; similar to what is observed in the

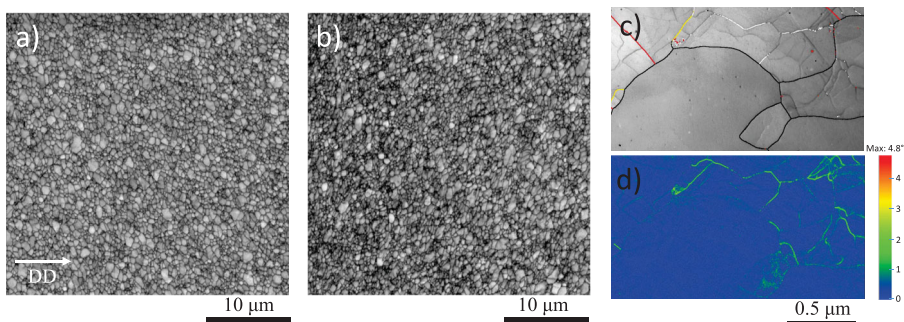


Figure 6. The band contrast EBSD images of (a) first layer and (b) last layer 316L stainless steel deposition. The TKD band contrast (c) and corresponding local misorientation (d) images of last layer deposition. The black, yellow, white and red lines in (c) represent boundaries with misorientation angles $>15^\circ$, $>10^\circ$, $>5^\circ$ and twin boundaries (i.e. $60^\circ/\langle 111 \rangle$), respectively. DD in (a) represents the deposition direction. To view this figure in colour, please visit the online version of the paper.

grain structure obtained at the tip of feedstock in the current study (Figure 2 (c)). Despite the similarity between FSW and AFSD processes as exhibited in overall texture (Figure 5), the current result reveals extensive grain refinement (i.e. $\sim 0.7 \mu\text{m}$), which is about two orders of magnitude smaller than what is reported for FSW processed materials (i.e. $40 \mu\text{m}$) with low-to-medium stacking fault energy undergoing discontinuous dynamic recrystallisation [21, 22].

In addition to the grain refinement differences, the misorientation angle distribution in deposited layers significantly differed from what is expected from a DDRX microstructure as observed in the region close to the pin (Figures 7 and 3(b)). Both the first and last deposited layers revealed a relatively similar distribution, having two moderate peaks at the positions of $\sim 45^\circ$ and 60° . In addition, the maxima at $\langle 111 \rangle$ in the misorientation axis distributions at 60° were broad and spread towards the $\langle 101 \rangle$ orientation (Figure 7), suggesting that the material experienced a large amount of plastic deformation. This is evident from the significant reduction in the length fraction of annealing twin boundaries in the deposited layers, to $5 \pm 0.1\%$ and $3.6 \pm 0.1\%$ for the first and last layers, respectively, compared with the as-received condition (i.e. $46 \pm 0.5\%$). Among these, the coherent twin boundaries were $2.4 \pm 0.1\%$ and $1.5 \pm 0.1\%$, and incoherent twin boundaries were $2.6 \pm 0.1\%$ and $2 \pm 0.1\%$ for the first layer and last layer, respectively. This observation along with the presence of strong shear texture (Figure 5) suggests that the grain refinement takes place through continuous dynamic recrystallisation (CDRX) rather than DDRX, as the microstructure is in a deformed state.

There are two main CDRX mechanisms operating during deformation, namely geometric CDRX and lattice rotation CDRX, depending on the material and thermomechanical conditions [23]. Geometric CDRX is strongly related to the amplitude of the boundary serrations, as new CDRX grains are formed

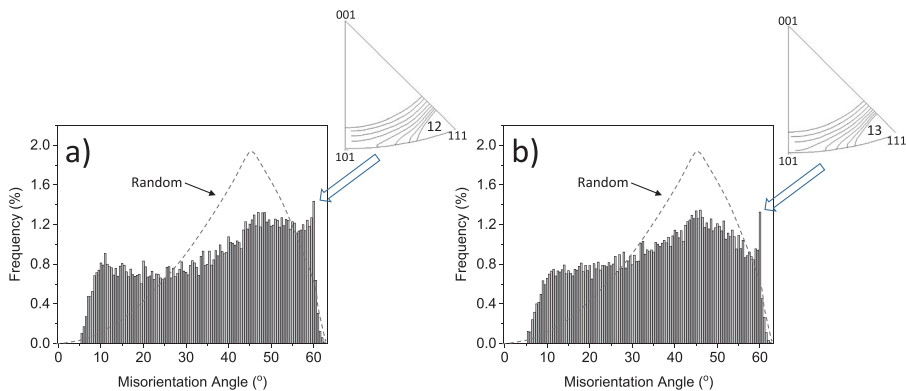


Figure 7. Misorientation angle distribution and the corresponding distribution of misorientation axes at a rotation of 60° in a standard stereographic triangle for (a) first layer and (b) last layer 316L stainless steel deposition. The dash line curve represents the random misorientation angle distribution.

through pinching off the serrated boundaries of elongated grains during deformation [23]. In the current study, the high angle boundaries were largely free of serrations (Figure 6(c)). This is not surprising as the grain boundary serration is strongly related to the deformation temperature (i.e. it increases with an increase in the deformation temperature) for a given strain [24]. Suh et al. has shown that no boundary serration appeared at a deformation temperature of 550°C (i.e. $\sim 0.5 T_m$) for a Ni-30Fe alloy with a moderate SFE [24].

However, a number of incomplete high angle boundaries were observed in the microstructure, which were usually connected to low angle boundaries delineating substructure/subgrain features (Figure 6). This appears to form through a progressive rotation of subgrains with respect to the surrounding region, as a local misorientation appeared on most sub-boundaries (Figure 6(c)). This is a typical microstructure observed during lattice rotation CDRX, where the deformation initially promotes dislocation rearrangement, leading to dislocation cell/subgrain substructure formation through dynamic recovery. This is then followed by strain-induced sub-boundary formation characterised by a relatively low misorientation angle, which is progressively converted to high-angle boundaries [23]. This ultimately results in the increase in the low-to-high angle boundary population, as observed in the current study (Figure 7). This observation differs from the Al-Mg-Si alloy with a high SFE deposited through AFSD, where the grain refinement takes place through both geometric and lattice rotation CDRX mechanisms [7]. However, similar observations were reported for the materials with low-to-medium SFE subjected to multi-directional forging [25] and warm rolling/compression [26], where the lattice rotation CDRX mechanism is dominant at a temperature range of $< \sim 0.6 T_m$ (i.e. warm deformation) under a relatively high strain rate condition. Therefore, the peak temperature during the deposition can be estimated to be $\sim 0.6 T_m$ in the current study, where the material is very susceptible to dynamic recovery, leading to the formation of a uniform polygonised substructure through rapid dislocation rearrangement, and the grain boundary serration is negligible.

It should be emphasized that local misorientations/subgrain boundaries also appear in some grain interiors formed through the DDRX process, as they progressively experience deformation upon their formation (Figure 2(c)). This feature is continuously replaced by new DDRX grains during further straining, resulting in the presence of a relatively high fraction of annealing twin boundaries (Figure 3(b)). However, the new equiaxed grains do not form through the conventional nucleation and growth (i.e. DDRX) in the CDRX process, and they are largely free of annealing twins and pre-existing twins are progressively distorted through their interaction with dislocations. As a result, the 60° misorientation peak observed in the as-received microstructure significantly diminishes, enhancing the population of boundaries with lower misorientation

angles in the deposited layers (Figure 1(a), Figure 7). This is a typical observation reported for materials undergoing CDRX [25, 26].

Grain boundary characteristics. The relative area distributions of grain boundary planes, irrespective of misorientation, were drawn in the crystal reference frame for the as-received and deposited microstructures. The distribution was quantified by multiples of a random distribution, where values greater than 1 mean that planes were observed more frequently than expected in a random distribution. The distribution for the as-received microstructure revealed a significant anisotropy with a maximum at the position of (111) planes having 4.78 MRD, suggesting that the (111) plane population was $\sim 380\%$ more than expected in a random distribution. The distribution had a minimum at the position of (001) and the intensity (101) orientation was ~ 1 MRD (Figure 8(a)). This is consistent with the observations by others, as (111) planes represent the low energy interfaces in FCC materials [27, 28].

For the first layer, the distribution revealed a peak at the position of (111) having an intensity of 1.46 MRD and spread towards (101) with 1.1 MRD (Figure 8(b)). The peak at (101) further intensified in the final layer, showing 1.24 MRD, which is comparable with the intensity at the (111) position (Figure 8(c)). The change in the distribution is related to the reduction in the population of annealing twin boundaries and the overall texture. In fact, the presence of a relatively strong $\langle 110 \rangle$ texture developed due to the shear deformation during deposition enhances the termination of planes with a (101) orientation. A similar behaviour was also reported for materials with strong {100} [29] and {111} [30] texture, where the boundaries with plane orientation of (100) and (111), respectively, were enhanced.

The grain boundary plane distribution for the boundaries with $60^\circ/[111]$ lattice misorientation (i.e. the first order annealing twin boundaries) displayed a strong peak at the $\{111\}/\{111\}$ twist position for all microstructures (Figure 9 (a, d, g)). This is not surprising as the (111) plane orientation correlates to the lowest energy in the distribution [27, 28]. However, the intensity of the peak was much greater in the as-received condition (i.e. ~ 2050 MRD) compared with the first and last layers having 83 MRD and 76 MRD, respectively

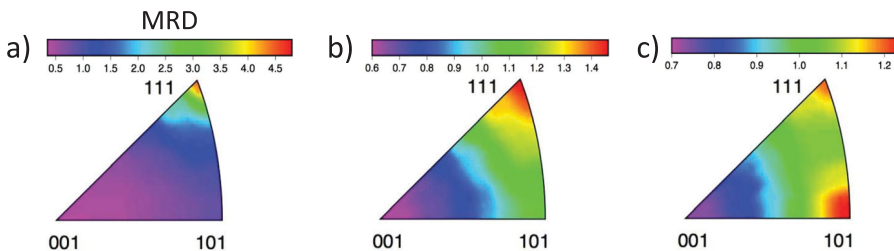


Figure 8. Grain boundary plane distributions, irrespective of misorientation, of (a) as-received (substrate), (b) first layer and (c) last layer 316L stainless steel deposition. MRD represents multiples of a random distribution. To view this figure in colour, please visit the online version of the paper.

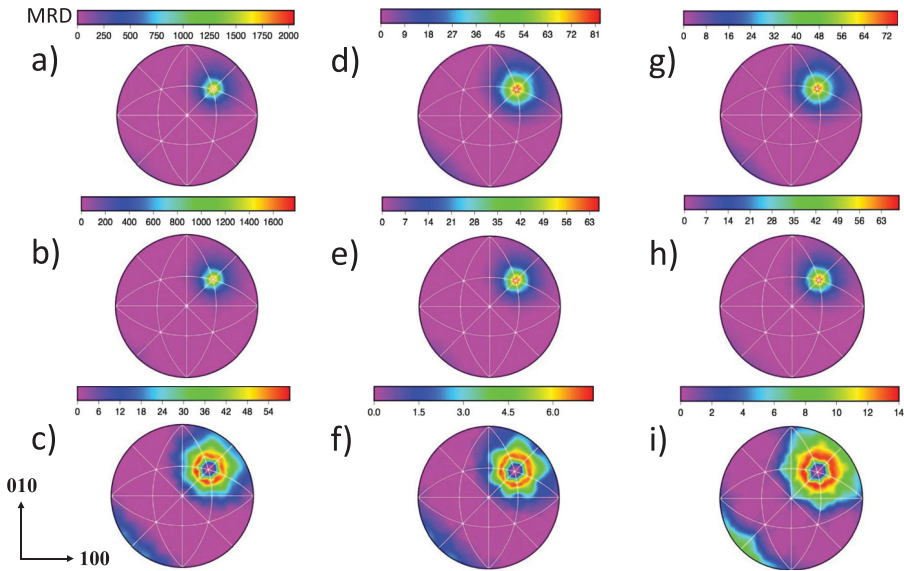


Figure 9. The distribution of plane normals for different types of $\Sigma 3$ boundaries (a, d, g) overall $\Sigma 3$, (b, e, h) coherent $\Sigma 3$ and (c, f, i) incoherent $\Sigma 3$ for (a–c) as-received, (d–f) first layer and (g–i) last layer 316L stainless steel deposition. MRD represents multiples of a random distribution. To view this figure in colour, please visit the online version of the paper.

(Figure 9(a, d, g)). This is due to a greater population of annealing twin boundaries in the as-received condition (i.e. $46 \pm 0.5\%$) than microstructures developed during the MELD process (i.e. $<5\%$).

For the first and last deposited layers, 48% and 42% of the twins were incoherent, compared to 11% in the as-received material. As expected, the distribution of coherent twin boundaries revealed a single peak at the (111) position for all microstructures (Figure 9(b, e, h)), though the incoherent twin boundaries displayed a ring around the (111) position (Figure 9(c, f, i)). However, it displayed more spread for the last layer compared with the first layer, suggesting the microstructure consisted of annealing twin boundaries with a greater incoherency (Figure 9(f, i)). The discrepancy between the first and last layer could be due to the strain-induced migration of boundaries in the absence of recrystallisation, which are driven by the thermal energy induced by deposition of the subsequent layers and the dislocation gradient within neighbouring grains in the deposited microstructure (i.e. reduction in dislocation density). This ultimately leads to the enhancement of boundaries with low energy interfaces through the dislocation removal (recovery) process, which is one of the grain boundary engineering mechanisms employed for FCC materials [31]. The enhancement of low energy boundaries through recovery ultimately increases the population of boundaries with a low energy (111) plane orientation at the expense of the (101) plane orientation in the first layer compared with the last layer deposited (Figure 8(b, c)).

Conclusions

The 3D printing was successfully conducted for 316L stainless steel through solid-state additive friction stir deposition. Detailed characterisation of the microstructure through the thickness led to the following conclusions:

- (1) The overall texture displayed shear components associated with FCC materials, consisting of strong B and \bar{B} orientations situated on the $\{hkl\}\langle 110\rangle$ fibre and a weaker A and \bar{A} components positioned along the $\{111\}\langle uvw\rangle$ fibre. However, the texture weakened in the middle of the block due to the complexity in deformation path during deposition.
- (2) The microstructure consisted of extremely fine equiaxed grains ($\sim 0.5\ \mu\text{m}$) along with a subgrain/substructure delineated by segments of high and low angle boundaries. This is typical of microstructures developed through continuous dynamic recrystallisation.
- (3) The microstructure was nearly uniform throughout the printed block, suggesting that the friction heat generated through the deposition of subsequent layers did not significantly alter the grain size of previously deposited layer/s.
- (4) The misorientation angle distribution of the deposited layers significantly differed from the as-received condition, as the imposed deformation significantly distorted the $\Sigma 3$ boundaries and introduced low angle boundaries, which progressively transformed to high angle misorientations through CDRX.
- (5) The AFSD process significantly reduced the anisotropy of the grain boundary plane distribution revealing two peaks at the position of the (111) and (110) orientations.

Acknowledgements

Deakin University's Advanced Characterisation Facility is acknowledged for use of the EBSD instruments.

Disclosure statement

No potential conflict of interest was reported by the author(s).

ORCID

Ehsan Farabi  <http://orcid.org/0000-0002-1127-5945>

References

- [1] D. Zhang, D. Qiu, M.A. Gibson, Y. Zheng, H.L. Fraser, D.H. St John and M.A. Easton, *Additive manufacturing of ultrafine-grained high-strength titanium alloys*. *Nature* 576 (2019), pp. 91–95.

- [2] C.J. Todaro, M.A. Easton, D. Qiu, M. Brandt, D.H. St John and M. Qian, *Grain refinement of stainless steel in ultrasound-assisted additive manufacturing*. *Add. Manuf.* 37 (2021), pp. 101632.
- [3] S. Yin, J. Cizek, X. Yan and R. Lupoi, *Annealing strategies for enhancing mechanical properties of additively manufactured 316L stainless steel deposited by cold spray*. *Surf. Coat. Technol.* 370 (2019), pp. 353–361.
- [4] T. Han, C.-H. Kuo, N. Sridharan, L.M. Headings, S.S. Babub and M.J. Dapino, *Effect of preheat temperature and post-process treatment on the microstructure and mechanical properties of stainless steel 410 made via ultrasonic additive manufacturing*. *Mater. Sci. Eng. A* 769 (2020), pp. 138457.
- [5] H.Z. Yu, M.E. Jones, G.W. Brady, R.J. Griffiths, D. Garcia, H.A. Rauch, C.D. Cox and N. Hardwick, *Scr. Mater.* 153 (2018), pp. 122–123.
- [6] MELD manufacturing, <https://www.meldmanufacturing.com>.
- [7] R.J. Griffiths, D. Garcia, J. Song, V.K. Vasudevan, M.A. Steiner, W. Cai and H.Z. Yu, *Solid-state additive manufacturing of aluminum and copper using additive friction stir deposition: Process-microstructure linkages*. *Materialia* 15 (2021), pp. 100967.
- [8] O.G. Rivera, P.G. Alison, J.B. Jordon, O.L. Rodriguez, L.N. Brewer, Z. McClelland, W.R. Wittington, D. Francis, J. Su, R.L. Martens and N. Hardwick, *Microstructures and mechanical behavior of Inconel 625 fabricated by solid-state additive manufacturing*. *Mater. Sci. Eng. A* 694 (2017), pp. 1–9.
- [9] G.S. Rohrer, D.M. Saylor, B.E. Dasher, B.L. Adams, A.D. Rollett and P. Wynblatt, *The distribution of internal interfaces in polycrystals*. *Zeitschrift für Metallkunde* 95 (2004), pp. 197–214.
- [10] B. Beausir and J.J. Fundenberger, *Analysis tools for electron and x-ray diffraction*, 2000; ATEX software available at www.Atex-Software.Eu.
- [11] S. Poulat, B. Decamps and L. Priester, *Weak-beam transmission electron microscopy study of dislocation accommodation processes in nickel $\Sigma 3$ grain boundaries*. *Philos. Mag.* A 77 (1998), pp. 1381–1397.
- [12] R.E. Schramm and R.P. Reed, *Stacking fault energies of seven commercial austenitic stainless steels*. *Metall. Trans. A* 6 (1975), pp. 1345–1351.
- [13] H. Beladi, I.B. Timokhina, Y. Estrin, J. Kim, B.C. De Cooman and S.K. Kim, *Orientation dependence of twinning and strain hardening behaviour of a high manganese twinning induced plasticity steel with polycrystalline structure*. *Acta Mater.* 59 (2011), pp. 7787–7799.
- [14] C. Chen, B. Lv, X. Feng, F. Zhang and H. Beladi, *Strain hardening and nanocrystallization behaviors in Hadfield steel subjected to surface severe plastic deformation*. *Mater. Sci. Eng. A* 729 (2018), pp. 178–184.
- [15] H. Beladi, P. Cizek and P.D. Hodgson, *On the characteristics of substructure development during dynamic recrystallization*. *Acta Mater.* 58 (2010), pp. 3531–3541.
- [16] L.S. Toth, P. Gilormini and J.J. Jonas, *Effect of rate sensitivity on the stability of torsion textures*. *Acta Metall.* 36 (1988), pp. 3077–3091.
- [17] R.W. Fonda and K.E. Knipling, *Texture development in friction stir welds*. *Sci. Technol. Weld. Join.* 16 (2011), pp. 288–294.
- [18] A.P. Zhilyaev and T.G. Langdon, *Using high-pressure torsion for metal processing: fundamentals and applications*. *Prog. Mater. Sci.* 53 (2008), pp. 893–979.
- [19] T. Pettersen and E. Nes, *On the origin of strain softening during deformation of aluminum in torsion to large strains*. *Metall. Mater. Trans. A* 34A(12) (2003), pp. 2727–2736.
- [20] F.C. Liu and T.W. Nelson, *In-situ grain structure and texture evolution during friction stir welding of austenite stainless steel*. *Mater. Des.* 115 (2017), pp. 467–478.

- [21] Y. Miyano, H. Fujii, Y. Sun, Y. Katada, S. Kuroda and O. Kamiya, *Mechanical properties of friction stir butt welds of high nitrogen-containing austenitic stainless steel*. Mater. Sci. Eng. A 528 (2011), pp. 2917–2921.
- [22] N. Kumar, M. Komarasamy, P. Nelaturu, Z. Tang, P.K. Liaw and R.S. Mishra, *Friction stir processing of high entropy alloy Al0.1CoCrFeNi*. JOM 67 (2015), pp. 1007–1013.
- [23] F.J. Humphreys and M. Hatherly, *Recrystallization and related annealing phenomena*, in F.J. Humphreys, M. Hatherly, eds., Elsevier, Oxford, 2004. pp. 67–89.
- [24] D.-W. Suh, T. Inoue, S. Torizuka, A. Ohmori and K. Nagai, *Serration of grain boundary in Ni-30Fe alloy through high temperature deformation*. ISIJ Int. 42 (2002), pp. 1026–1032.
- [25] J. Huang and Z. Xu, *Evolution mechanism of grain refinement based on dynamic recrystallization in multiaxially forged austenite*. Mater. Lett. 60 (2006), pp. 1854–1858.
- [26] M. Tikhonova, R. Kaibyshev and A. Belyakov, *Microstructure and mechanical properties of austenitic stainless steels after dynamic and post-dynamic recrystallization treatment*. Adv. Eng. Mater. 20 (2018), pp. 1700960.
- [27] H. Beladi, N.T. Nuhfer and G.S. Rohrer, *The five parameter grain boundary character and energy distributions in a fully austenitic high manganese steel using three dimensional data*. Acta Mater. 70 (2014), pp. 281–289.
- [28] J. Li, S.J. Dillon and G.S. Rohrer, *Relative grain boundary area and energy distributions in nickel*. Acta Mater. 57 (2009), pp. 4304–4311.
- [29] T. Watanabe, *Toughening of brittle materials by grain boundary design and control*. Mater. Sci. Forum 126-128 (1993), pp. 295–304.
- [30] H. Beladi and G.S. Rohrer, *The role of thermomechanical routes on the distribution of grain boundary and interface plane orientations in transformed microstructures*. Metall. Mater. Trans. A 48 (2017), pp. 2781–2790.
- [31] V. Randle, *Mechanism of twinning-induced grain boundary engineering in low stacking-fault energy materials*. Acta Mater. 47 (1999), pp. 4187–4196.